Cement and Concrete Research 41 (2011) 102–106

Contents lists available at ScienceDirect

Cement and Concrete Research

journal homepage: http://ees.elsevier.com/CEMCON/default.asp

Does the Al substitution in C–S–H(I) change its mechanical property?

Jae Eun Oh [a], Simon M. Clark [b,c], Paulo J.M. Monteiro [a,*]

[a] Department of Civil and Environmental Engineering, University of California, Berkeley, CA 94720, USA
[b] Advanced Light Source, Lawrence Berkeley National Laboratory, Berkeley, California CA 20015, USA
[c] Department of Earth and Planetary Sciences, University of California, Berkeley, CA 94720, USA

ARTICLE INFO

Article history:
Received 19 May 2010
Accepted 22 September 2010

Keywords:
Calcium silicate hydrate (C–S–H)
X-ray diffraction
Elastic moduli
Mechanical properties
Alkali-activated cement

ABSTRACT

This study examines the influence of Al substitution for Si on the bulk modulus of calcium silicate hydrate I [C–S–H(I)], a structural analogue of C–S–H, by performing high-pressure synchrotron X-ray diffraction experiments in two C–S–H(I) samples: one a hydration product of alkali-activated slag and the other a synthetic C–S–H(I). The test result shows that not only the bulk modulus but also the incompressibility of the lattice parameters *a*, *b*, and *c* of two C–S–H(I) samples are very similar to each other, regardless of the Al substitution. This result may be due to the four-coordinated configuration of the substituted Al, which makes the dreierketten silicate chains maintain the same arrangement after the substitution.

1. Introduction

There is a general agreement that the main reaction product of alkali-activated slag cement (AAS) is calcium silicate hydrate (C–S–H); however, it has a much lower Ca/Si ratio (= 0.8 ~ 1.5) and is more crystalline than the C–S–H found in hydrated portland cement paste [1], consequently implying that the main reaction product of AAS is C–S–H(I) [2,3].

Besides its importance as a reaction product of AAS, C–S–H(I) has also gained significance in fundamental research because it has been viewed as an imperfect form of tobermorite in the C–S–H structural model [1]; that is, both C–S–H(I) and tobermorite resemble C–S–H with respect to their crystal structure [hereafter, we will call the chemically synthesized C–S–H(I) as SYN C–S–H(I) to distinguish the C–S–H(I) from AAS, which will hereafter be called AAS C–S–H(I)].

The major structural difference between SYN C–S–H(I) and AAS C–S–H(I) is the Al substitution for Si [frequently observed in AAS C–S–H(I)], which occurs predominantly at the bridging tetrahedral sites in dreierketten silicate chains in AAS (see Fig. 1), as confirmed by NMR studies [3–8].

The presence of other minor reaction products largely varies, depending on the sources of blast furnace slag and the types of alkali-activating solutions. Common minor reaction products include the hydrotalcite-like phase, the Fe-rich hydrogarnet phase, and the ettringite, $Ca(OH)_2$, and AFm phases [3–5,9]. The hydrotalcite-like phase has been found to coexist intermixed with AAS C–S–H(I) and has an approximate atomic ratio of Mg/Al = 2.1 [3], 2.55 [5], or 2.3 [10] although a theoretical atomic Mg/Al ratio of hydrotalcite [$Mg_6Al_2CO_3(OH)_{16}\cdot 4H_2O$] is 3.0. Thus, some portion of Al found in AAS C–S–H(I) phase is consumed by the hydrotalcite-like phase and should be excluded in the calculation of Al/Si ratio in AAS C–S–H(I).

Earlier studies have reported atomic Al/Si ratios (or Al/Ca) in AAS C–S–H(I) as 0.11 ~ 0.34, which seems to be somewhat independent of hydration time [3,5,6,10–12]. The dreierketten silicate chains in C–S–H and C–S–H(I) resemble the long chains of tobermorite (see Fig. 1); however, the chains form fragments having 2, 5, 8, …, (3n − 1) tetrahedra [1]. In real C–S–H, the dimers are the most predominant silicate chains [13], whereas in AAS C–S–H(I) and SYN C–S–H(I), pentamers are the most dominant chains [5,6,14]. When we assume that only pentameric silicate chains exist in AAS C–S–H(I) and Al substitution occurs dominantly at middle bridging tetrahedral sites, the value Al/Si = 0.11 in AAS C–S–H(I) indicates that approximately 50% of bridging tetrahedral sites are taken by tetrahedral Al atoms, and the Al/Si = 0.25 implies 100% of substitution of Al for bridging Si. Therefore, the Al/Si ratio = 0.11 ~ 0.34 indicates a high degree of Al substitution ratio in the AAS C–S–H(I) structure.

No study has investigated a possible change of the mechanical properties of C–S–H(I) attributed to the Al substitution although many papers discussed the Al substitution in AAS C–S–H(I) [3,5–7]. This study presents bulk modulus values of two different C–S–H(I) samples [i.e., SYN C–S–H(I) and AAS C–S–H(I)] using high-pressure synchrotron X-ray diffraction and discusses the effect of Al substitution on the bulk modulus of C–S–H(I). Note that AAS C–S–H(I) was a real hydration product and its hardened AAS paste showed a compressive strength of 49 MPa at 14 days of curing. Accordingly, the measured bulk modulus of AAS C–S–H(I) of the current study can

* Corresponding author.
E-mail address: monteiro@berkeley.edu (P.J.M. Monteiro).

0008-8846/$ – see front matter © 2010 Published by Elsevier Ltd.
doi:10.1016/j.cemconres.2010.09.010

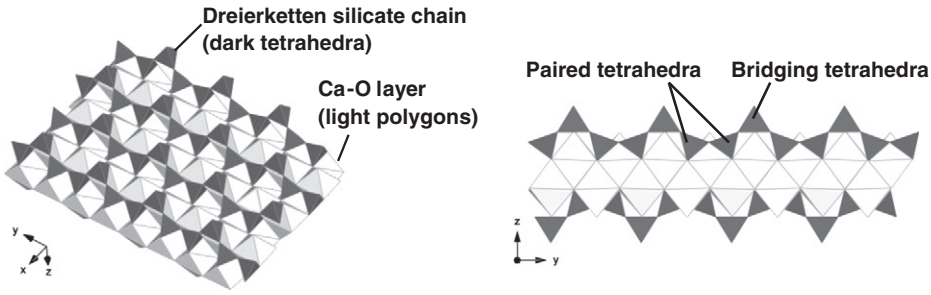

Fig. 1. Schematic views of dreierketten silicate chains and Ca–O layer found in tobermorite, an analogue of C–S–H(I). C–S–H(I) has very similar Ca–O layer structures with tobermorite but the length of silicate chains is much shorter. The Al substitution for Si occurs predominantly at the bridging tetrahedral sites.

be directly used for any mechanical simulation study of alkali-activated slag cement.

2. Experimental program

The SYN C–S–H(I) sample [Ca/Si = 0.97(6), probed by electron microprobe] was purchased from Construction Technology Laboratories and the AAS C–S–H(I) sample [Ca/Si = 0.96(6), Al/Si = 0.34 (3) probed by energy-dispersive spectroscopy] was directly synthesized by the alkali activation of ground blast furnace slag by a high concentration (= 10 M) of NaOH solution using a water bath after 40 days of curing (solution/binder weight ratio = 0.4, curing temperature = 80 °C for the whole curing duration; see Table 1). The alkali-activated slag sample showed a compressive strength of 49 MPa at 14 days of curing.

All high-pressure X-ray diffraction experiments were carried out at beamline 12.2.2 of the Advanced Light Source [15]. For the experiments, a synchrotron monochromatic X-ray beam with λ = 0.4959 Å (= 25-keV energy) was used. LaB6 powder was used for the calibration of working distance between a sample and a detector. Diffraction patterns were recorded with a MAR345 image plate (3 450 × 3 450 pixels), with an exposure time of 300 s in a room temperature and analyzed with the FIT2D [16], XFIT [17].

All samples were finely ground and mixed with a pressure-transmitting liquid medium (4:1 methanol/ethanol solution), placed into a small sample chamber of a steel gasket in the diamond anvil cell (DAC; see Fig. 2). The utilized sample chamber size was 180 μm in diameter, with a 63-μm thickness. The pressure inside the sample chamber was determined using the ruby (Al_2O_3 doped with Cr^{3+} (0.05%)) fluorescence calibration method [18].

3. Results and discussion

Figs. 3 and 4 show the powder X-ray diffraction patterns of two C–S–H(I) samples as a function of pressure and the changes in unit cell parameters are summarized as a function of pressure in Tables 2 and 3.

A major experimental difficulty was that the structure of C–S–H(I) has not been solved mainly due to its poor crystallinity. No atom coordinates and no space group information of C–S–H(I) have been revealed, but only (*hkl*) indexing for diffraction pattern and its crystal system (= orthorhombic) are currently available [1,19]. Consequently, structural refinement of unit cell parameters was not possible. Furthermore, most of the diffraction peaks of C–S–H(I) samples rapidly merged into the background above pressure of about 1 ~ 1.5 GPa and were not measurable above about 4 GPa, and thus, correctly indexing all of the peaks in the diffraction pattern was challenging. Given these difficulties, the unit cell parameters were manually calculated using only three major distinct diffraction peaks of C–S–H(I), which survived over the measured pressure range. In order to maximize the reliability of calculation, only the most consistently distinguishable peaks were chosen by careful comparison of the data with the values reported in the literature. All peaks that had ambiguities in their identification were excluded from our calculations of lattice parameters and unit cell volumes. This condition left only three peaks for each of the C–S–H(I) phases, from which we could calculate unit cell parameters. For SYN C–S–H(I), the (002), (400), and (040) reflections were used, and for AAS C–S–H(I), the (002), (220), and (400) reflections were used. Despite these experimental difficulties, reasonable values for lattice parameters and unit cell volumes were obtained.

A third-order Birch–Murnaghan equation of state was fitted to the pressure-normalized volume data to obtain a bulk modulus values and the equation is expressed as

$$P = \frac{3}{2}K_o\left[(V/V_o)^{-\frac{7}{3}} - (V/V_o)^{-\frac{5}{3}}\right]\left[1 + \frac{3}{4}(K_o' - 4)\left((V/V_o)^{-\frac{2}{3}} - 1\right)\right]$$

where V is the volume of unit cell under increased pressure, V_o is the initial volume of unit cell at ambient pressure, P is the pressure applied to the material, K_o is the bulk modulus at zero pressure and K_o' is the pressure derivative of bulk modulus at zero pressure [20].

By defining the normalized pressure, $F = P/\{1.5[(V/V_o)^{-7/3} - (V/V_o)^{-5/3}]\}$, and the Eulerian strain, $f = 0.5 \cdot ((V/V_o)^{-2/3} - 1)$, the third-order Birch–Murnaghan equation of state is reorganized into the following linear form: $F(f) = K_o - 1.5K_o(4 - K_o')f$.

In the plot of F versus f, the y-intercept and the slope of the weighted least-squares fit gives the bulk modulus K_o and its pressure derivative K_o' at zero pressure. Note that the pressure derivative K_o' for many materials approach 4, and thus, it is quite often assumed that K_o' is 4 for low-range-pressure studies [21] and high-pressure zeolite studies [22], as assumed in the present study. A weighted linear least-squares fit with errors [23] was used to modify the standard least-squares regression to reduce any erroneous effects. The fitted curves of the equation of state with experimental data are depicted in Fig. 5. The bulk modulus (K_o) and the pressure derivatives (K_o') using the f–F plot are presented in Table 4.

The AAS C–S–H(I) sample had a large amount of Al substitution (~0.34 for the current sample by EDS) [5–7,10], whereas the SYN C–S–H(I) sample did not contain any Al. Nevertheless, as shown in Fig. 5 and Table 4, the pressure-normalized volume compression curves and bulk modulus values for the two C–S–H(I) samples are

Table 1
Chemical compositions (%) and atomic ratios of the ground blast furnace slag used for synthesizing C–S–H(I).

SiO_2	Al_2O_3	Fe_2O_3	CaO	MgO	Na_2O	K_2O	TiO_2	P_2O_5	MnO	Total	Al/Si	Ca/Si
33.04	13.35	0.18	41.78	6.02	0.20	0.37	1.15	0.02	0.35	96.89	0.48	1.35

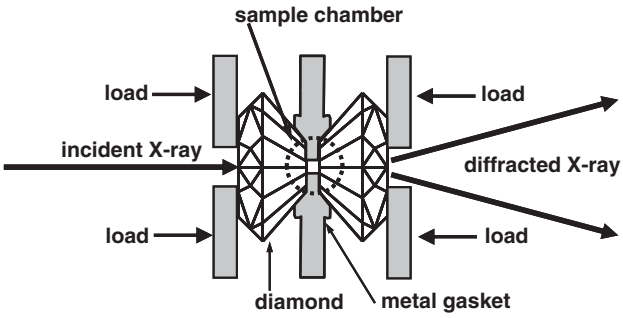

Fig. 2. Schematic view of high-pressure X-ray diffraction using a diamond anvil cell.

seen to be very similar. Moreover, the incompressibility of lattice parameters *a*, *b*, and *c* are seen almost identical between the two C–S–H(I) samples, as shown in Fig. 6, implying that the Al substitution seems to have little effect on the incompressibility of C–S–H(I). In addition, it is interesting that all the incompressibilities of a/a_o and b/b_o for the two C–S–H(I) samples are on the same curve, implying that the in-plane incompressibility of the CaO plane of C–S–H(I) are independent of the *a*- and *b*-directions.

The value of bulk modulus obtained using the third-order Birch–Murnaghan equation of state may be distorted when one uses an incorrect ambient pressure–volume data because the *f*–*F* plot is highly sensitive to the ambient data. This problem may occur in the present study because the powder sample used in the DAC measurement was not the same as the sample used in the ambient test although they are from the same sample source. However, it is possible to avoid this limitation by using the *g*–*G* plot [24], which makes it possible to obtain the bulk modulus of third-order Birch–Murnaghan equation of state using only the data measured under high pressure without a measured ambient pressure–volume data. The calculated bulk modulus values using the *g*–*G* plot are presented in Table 5, which shows a little higher values than those obtained using the *f*–*F* plot;

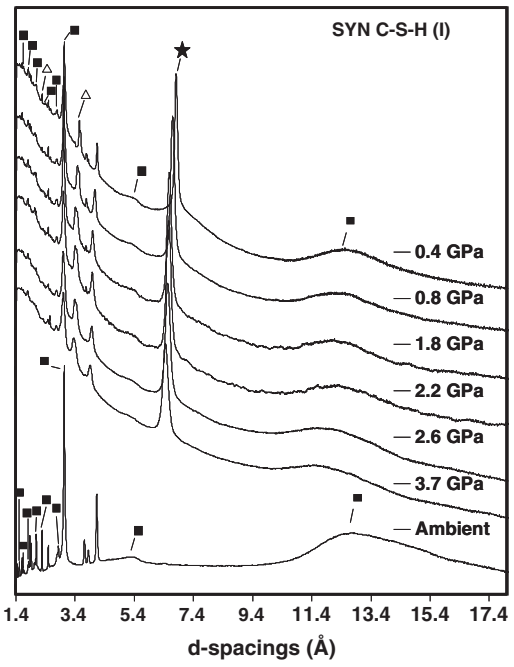

Fig. 3. Diffraction patterns with increasing pressure from the SYN C–S–H(I) sample. The solid squares (■) in the figure show diffraction peaks for C–S–H(I) (JCPDS card #34-0002 and [1,19]). The Δ symbols denote ruby (corundum). The peak with the symbol ★ indicates an externally oriented X-ray diffraction peak from outside the sample, which was not shown in the ambient diffraction pattern.

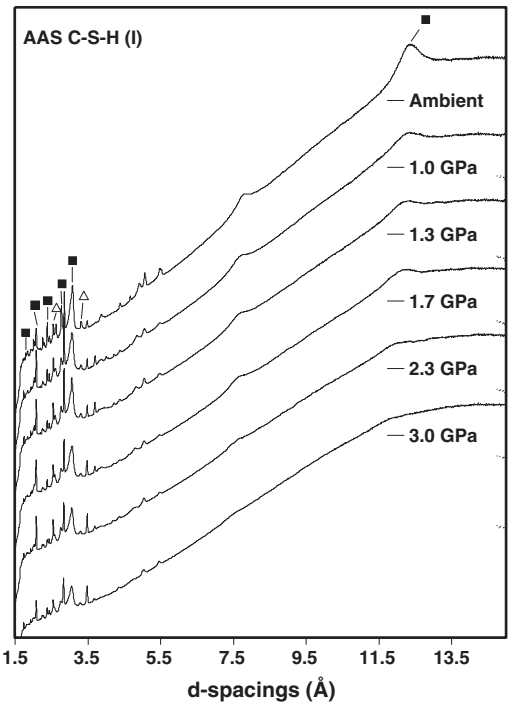

Fig. 4. Diffraction patterns with increasing pressure from the AAS C–S–H(I) sample. The solid squares (■) in the figure show diffraction peaks for C–S–H(I) (JCPDS card #34-0002 and [1,19]). The Δ symbols denote ruby (corundum).

however, it still produced similar bulk modulus values between SYN C–S–H(I) and AAS C–S–H(I).

The similar incompressibility of the two C–S–H(I) samples, irrespective of the Al substitution, is possibly explained by the aluminum's tetrahedral configuration in the dreierketten silicate chains of C–S–H(I) [3,5–7,12]. Although Al substitutions occur in the silicate chains of C–S–H(I), the overall structural conformation of the dreierketten chains should have the same arrangement as in prior to the substitution because the substituted Al atoms remained in the tetrahedral configuration. Given the observation, therefore, the topology of silicate chains seems predominant in determining the bulk modulus rather than the species of elements composing the dreierketten chains. Similar occasions have been observed in high-pressure experiments for obtaining the bulk modulus of zeolites under high pressure [22]. In the high-pressure studies on zeolites, the topology of the zeolite framework structure consisting of tetrahedral Si and Al atoms are the dominant factors for determining the bulk modulus, rather than their chemical compositions or framework density [22], because the bond lengths of Al–O and Si–O should be constant [25] against the increasing external pressure and the volume change of the unit cell is mainly governed by the tilting of AlO_2 or SiO_2 tetrahedra [26]; likewise, the substitution of Al for Si may not significantly affect its structural topology of dreierketten silicate chains in the C–S–H(I) and its bulk modulus.

Table 2
Pressure–volume data with unit cell parameters for SYN C–S–H(I) as a function of hydrostatic pressure.

P (GPa)	V (Å^3)	a (Å)	b (Å)	c (Å)
Ambient	2078 ± 5	11.20 ± 0.02	7.312 ± 0.004	25.389 ± 0.005
0.4 ± 0.1	2053 ± 2	11.159 ± 0.004	7.290 ± 0.005	25.238 ± 0.003
0.8 ± 0.2	2014 ± 4	11.133 ± 0.009	7.28 ± 0.01	24.846 ± 0.003
1.8 ± 0.2	1974 ± 10	11.10 ± 0.02	7.26 ± 0.03	24.485 ± 0.009
2.2 ± 0.2	1983 ± 7	11.11 ± 0.01	7.24 ± 0.02	24.644 ± 0.007
2.6 ± 0.3	1953 ± 4	11.084 ± 0.008	7.24 ± 0.01	24.330 ± 0.003
3.7 ± 0.3	1906 ± 4	11.051 ± 0.010	7.22 ± 0.02	23.891 ± 0.003

Table 3
Pressure–volume data with unit cell parameters for AAS C–S–H(I) as a function of hydrostatic pressure.

P (GPa)	V (Å^3)	a (Å)	b (Å)	c (Å)
Ambient	1705 ± 4	11.130 ± 0.002	6.15 ± 0.01	24.88 ± 0.01
1.0 ± 0.2	1658 ± 3	11.066 ± 0.002	6.133 ± 0.008	24.43 ± 0.02
1.3 ± 0.2	1647 ± 0.9	11.056 ± 0.001	6.122 ± 0.002	24.33 ± 0.01
1.7 ± 0.2	1632 ± 6	11.052 ± 0.002	6.12 ± 0.02	24.135 ± 0.009
2.3 ± 0.2	1605 ± 7	11.024 ± 0.002	6.11 ± 0.04	23.81 ± 0.01
3.0 ± 0.3	1590 ± 10	11.009 ± 0.004	6.09 ± 0.04	23.66 ± 0.02

Table 4
Measured bulk modulus values of C–S–H(I) samples using the *f*–*F* plot. The calculation of K'_o for SYN C–S–H(I) was not satisfactory because the value turned out too high [= 13 (7)].

Phase	Bulk modulus K_o (GPa)	Pressure derivative K'_o (GPa)	*R*-squared value (R^2) of EOS to the data
SYN C-S-H (I)	34 ± 7	4.0 (assumed)	0.967
AAS C-S-H (I)	35 ± 3	4.0 (assumed)	0.992
	33 ± 6	6 ± 3 (calculated)	0.994

Atomistic simulations are making significant contributions in our understanding of C–S–H. Simulation studies of C–S–H tend to start from one of the crystalline tobermorite structures, adjust the interlayer distance, and then relax the structure. For example, lattice dynamics simulations by Gmira et al. [27] based on the structural models of 11-Å tobermorite by Merlino et al. [28] and Hamid et al. [29] but with an increased basal spacing of ~12 Å, which corresponds to the basal spacing of C–S–H(I), gave a bulk modulus of tobermorite-like C–S–H of 71.8 GPa. A potential energy minimization study by Pellenq et al. [30] using the same software package of Gmira et al. [27] gave a similar value for a bulk modulus of 61.9 GPa. Both of these studies gave bulk moduli that are far closer to the values for tobermorite than for C–S–H(I) as might be expected, given that these studies did not significantly disturb the basic tobermorite atomic structure but only modified the interlayer region. One might expect that adding structural disorder in the sheet structure (for example, by adding random omissions of bridging tetrahedra in the silicate dreierketten chains) would lead to a model that more closely resembles that of C–S–H. Manzano et al. [31] introduced such structural defects into the crystal structure of 14-Å tobermorite, thereby limiting the length of silicate chains [32] to the range from dimers to pentamers. This approach modified their calculated bulk modulus from 46 GPa for the 14-Å tobermorite to 21–29 GPa for C–S–H, which is slightly lower than our measured value. Manzano et al. [33] similarly simulated a bulk modulus of tobermorite-like structure with shortened silicate chains and obtained 33.7 GPa for the case of pentameric chains (Ca/Si = 1.00) and 36.8 GPa for the case of octameric chains (Ca/Si = 0.94). These results are consistent with the values of the current study.

A recent C–S–H model derived by energy minimization from an anhydrous 11-Å tobermorite followed by Monte Carlo simulation to determine water absorption [29] has been shown to give good agreement with literature EXAFS, diffraction, and chemical composition data for C–S–H but yielded a bulk modulus of 47–51 GPa. Again, this result is clearly higher than the result that we found for C–S–H(I) but this difference might be due to different Ca/Si ratios. The sample that we used had a low Ca/Si ratio while the system studied in this simulation has a high Ca/Si ratio. This case is hard to judge since the effect of Ca/Si ratio on the elastic properties of C–S–H is not clear, with some groups seeing an increase in elastic moduli with the Ca/Si ratio [32] and other groups seeing no change [31] Similarly, most of the existing experimental research using nanoindentation of C–S–H has

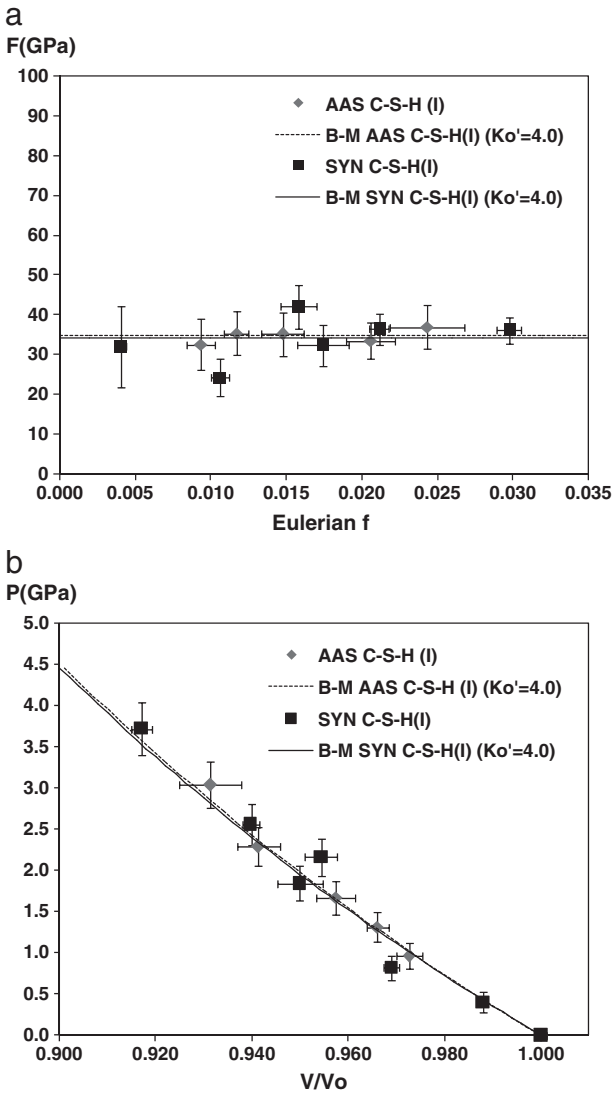

Fig. 5. (a) *f*–*F* plots for SYN C–S–H(I) and AAS C–S–H(I). (b) Pressure-normalized volume data of two C–S–H(I) samples with plots of third-order Birch–Murnaghan equation of state (B–M).

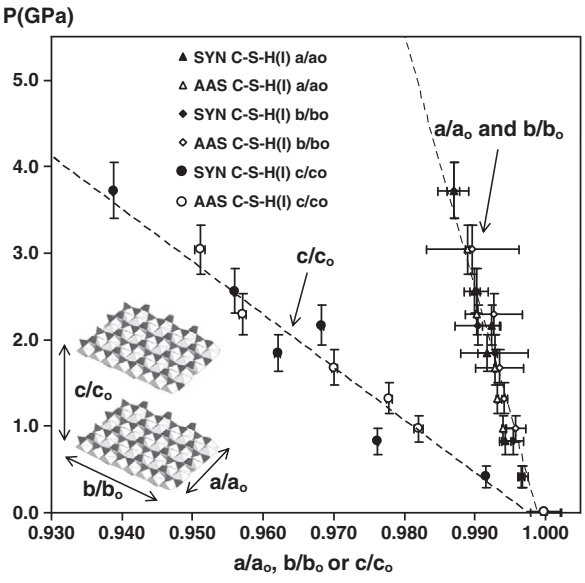

Fig. 6. Incompressibility of lattice parameters *a*, *b*, and *c* of the C–S–H(I) samples.

Table 5
Bulk modulus of C–S–H(I) samples using the *g*–*G* plot [24].

Phase	Bulk modulus K_o (GPa)	Pressure derivative K'_o (GPa)	*R*-squared value (R^2) of EOS to the data
SYN C–S–H(I)	38 ± 7	4.0 (assumed)	0.973
	34 ± 7	7 ± 7 (calculated)	0.972
AAS C–S–H(I)	38 ± 3	4.0 (assumed)	0.994
	38 ± 3	3 ± 3 (calculated)	0.994

been focused on samples containing high Ca/Si ratio so it is difficult to make a direct comparison to our results [34–38].

Plassard et al. [39] performed a comprehensive research on the effect of Ca/Si ratio on the elastic modulus perpendicular to the C–S–H layer plane. For low Ca/Si ratios, they obtained a value of 34.2 GPa. Assuming a Poisson' ratio of 0.25 for CSH, our experimental results give an elastic modulus of 57 GPa, apparently much higher than the result of Plassard et al. However, it should be noted that our results reflect an average value of elastic modulus while Plassard's results represent the value perpendicular to the layer plane. As shown in Fig. 6, the stiffness perpendicular to the layer plane is much lower than in the other directions so the results are consistent.

4. Conclusion

In the present study, we experimentally determined the bulk moduli of SYN C–S–H(I) and AAS SYN C–S–H(I)] using high-pressure synchrotron X-ray diffraction. The bulk modulus and incompressibility of lattice parameters are shown to be very similar between the two C–S–H(I) samples, strongly suggesting that the structural modifications that resulted from the Al substitution in C–S–H(I) do not significantly affect the bulk modulus of C–S–H(I). This result may be due to the substituted Al's four-coordinated configuration, which makes the overall structural conformation of the dreierketten chains remain the same as in prior to the substitution. This also suggests that the topology of silicate chains seems predominant in determining the bulk modulus, rather than the species of elements composing the dreierketten chains. Since the AAS C–S–H(I) sample was a real hydration product resulting in its hardened AAS paste, showing a high strength of 49 MPa at 14 days of curing, the measured bulk modulus of AAS C–S–H(I) in the current study can be directly used for any mechanical simulation study of alkali-activated slag cement.

Acknowledgements

This publication was based on work supported in part by Award No. KUS-l1-004021, made by King Abdullah University of Science and Technology (KAUST). The Advanced Light Source is supported by the Director, Office of Science, Office of Basic Energy Sciences, of the U.S. Department of Energy under Contract No. DE-AC02-05CH11231.

References

[1] H.F.W. Taylor, Cement chemistry, Thomas Telford, 1997.
[2] C. Shi, P.V. Krivenko, D.M. Roy, Alkali-activated cements and concretes, Taylor & Francis, 2006.
[3] S.D. Wang, K.L. Scrivener, Hydration products of alkali-activated slag cement, Cem. Concr. Res. 25 (1995) 561–571.
[4] D.M. Roy, Alkali-activated cements opportunities and challenges, Cem. Concr. Res. 29 (1999) 249–254.
[5] I. Richardson, A. Brough, G. Groves, C. Dobson, The characterization of hardened alkali-activated blast-furnace slag pastes and the nature of the calcium silicate hydrate(C–S–H) phase, Cem. Concr. Res. 24 (1994) 813–829.
[6] I.G. Richardson, A.R. Brough, R. Brydson, G.W. Groves, C.M. Dobson, Location of aluminum in substituted calcium silicate hydrate(C–S–H) gels as determined by ^{29}Si and ^{27}Al NMR and EELS, J. Am. Ceram. Soc. 76 (1993) 2285–2288.
[7] S.D. Wang, K.L. Scrivener, ^{29}Si and ^{27}Al NMR study of alkali-activated slag, Cem. Concr. Res. 33 (2003) 769–774.
[8] P. Faucon, T. Charpentier, A. Nonat, J.C. Petit, Triple-quantum two-dimensional ^{27}Al magic-angle nuclear magnetic resonance study of the aluminum incorporation in calcium silicate hydrates, J. Am. Chem. Soc. 120 (1998) 12075–12082.
[9] W. Chen, H.J.H. Brouwers, The hydration of slag: Part 1—Reaction models for alkali-activated slag, J. Mater. Sci. 42 (2007) 428–443.
[10] A.R. Brough, A. Atkinson, Sodium-silicate-based, alkali-activated slag mortars: Part I—Strength, hydration and microstructure, Cem. Concr. Res. 32 (2002) 865–879.
[11] I. Richardson, The nature of CSH in hardened cements, Cem. Concr. Res. 29 (1999) 1131–1147.
[12] P.J. Schilling, L.G. Butler, A. Roy, H.C. Eaton, ^{29}Si and ^{27}Al MAS NMR of NaOH-activated blast-furnace slag, J. Am. Ceram. Soc. 77 (2005) 2363–2368.
[13] X. Cong, R.J. Kirkpatrick, ^{29}Si MAS NMR study of the structure of calcium silicate hydrate, Adv. Cem. Based Mater. 3 (1996) 144–156.
[14] M. Grutzeck, A. Benesi, B. Fanning, Silicon^{-29} magic-angle-spinning nuclear magnetic resonance study of calcium silicate hydrates, J. Am. Ceram. Soc. 72 (2005) 665–668.
[15] M. Kunz, A.A. MacDowell, W.A. Caldwell, D. Cambie, R.S. Celestre, E.E. Domning, R.M. Duarte, A.E. Gleason, J.M. Glossinger, N. Kelez, D.W. Plate, T. Yu, J.M. Zaug, H.A. Padmore, R. Jeanloz, A.P. Alivisatos, S.M. Clark, A beamline for high-pressure studies at the Advanced Light Source with a superconducting bending magnet as the source, J. Synchrotron Radiat. 12 (2005) 650–658.
[16] A.P. Hammersley, Fit2d version 12.040, ESRF, Grenoble, France, 2006.
[17] 17.R.W. Cheary, A.A. Coelho. Programs XFIT and FOURYA, deposited in CCP14 Powder Diffraction Library, Engineering and Physical Sciences Research Council, Daresbury Laboratory, Warrington, England, (1996) (http://www.ccp14.ac.uk/tutorial/xfit-95/xfit.htm).
[18] H.K. Mao, J. Xu, P.M. Bell, Calibration of the ruby pressure gauge to 800 kbar under quasi-hydrostatic conditions, J. Geophys. Res. 91 (1986) 4673–4676.
[19] L. Heller, H.F.W. Taylor, Crystallographic data for the calcium silicates, HM Stationery Off., 1956.
[20] F. Birch, Elasticity and internal constitution of the Earth's interior, J. Geophys. Res. 57 (1952) 227–286.
[21] E. Knittle, Static compression measurements of equations of state, Mineral Physics and Crystallography: A Handbook of Physical Constants, 1995, pp. 98–142.
[22] G.D. Gatta, Does porous mean soft? On the elastic behaviour and structural evolution of zeolites under pressure, Z. Kristallogr. 223 (2008) 160–170.
[23] B.C. Reed, Linear least-squares fits with errors in both coordinates, Am. J. Phys. 57 (1989) 642–646.
[24] R. Jeanloz, Finite-strain equation of state for high-pressure phases, Geophys. Res. Lett. 8 (1981) 1219–1222.
[25] I. Hassan, H.D. Grundy, The crystal structures of sodalite-group minerals, Acta Crystallogr. Sect. B: Struct. Sci. 40 (1984) 6–13.
[26] S.E. Latturner, J. Sachleben, B.B. Iversen, J. Hanson, G.D. Stucky, Covalent guest–framework interactions in heavy metal sodalites: Structure and properties of thallium and silver sodalite, J. Phys. Chem. B 103 (1999) 7135–7144.
[27] A. Gmira, M. Zabat, R.J.M. Pellenq, H. van Damme, Microscopic physical basis of the poromechanical behavior of cement-based materials, Mater. Struct. 37 (2004) 3–14.
[28] S. Merlino, E. Bonaccorsi, T. Armbruster, The real structure of tobermorite 11A: Normal and anomalous forms, OD character and polytypic modifications, Eur. J. Mineralog. 13 (2001) 577–590.
[29] S. Hamid, The crystal structure of the 11A natural tobermorite Ca225 [Si3075 (OH) l. 5]–1H20, Z. Kristallogr. 154 (1981) 189–198.
[30] R.J.M. Pellenq, N. Lequeux, H. Van Damme, Engineering the bonding scheme in CSH: The iono-covalent framework, Cem. Concr. Res. 38 (2008) 159–174.
[31] H. Manzano, J. Dolado, A. Guerrero, A. Ayuela, Mechanical properties of crystalline calcium silicate hydrates: Comparison with cementitious CSH gels, Phys. Stat. Solid. 204 (2007) 1775–1780.
[32] E. Bonaccorsi, S. Merlino, A.R. Kampf, The crystal structure of tobermorite 14 Å (Plombierite): A C–S–H phase, J. Am. Ceram. Soc. 88 (2005) 505–512.
[33] H. Manzano, J. Dolado, A. Ayuela, Elastic properties of the main species present in Portland cement paste, Acta Mater. 57 (2009) 1666–1674.
[34] F.J. Ulm, G. Constantinides, F.H. Heukamp, Is concrete a poromechanics materials?—A multiscale investigation of poroelastic properties, Mater. Struct. 37 (2004) 43–58.
[35] G. Constantinides, F.J. Ulm, The effect of two types of CSH on the elasticity of cement-based materials: Results from nanoindentation and micromechanical modeling, Cem. Concr. Res. 34 (2004) 67–80.
[36] G. Constantinides, F.J. Ulm, K. Van Vliet, On the use of nanoindentation for cementitious materials, Mater. Struct. 36 (2003) 191–196.
[37] P. Mondal, S.P. Shah, L. Marks, A reliable technique to determine the local mechanical properties at the nanoscale for cementitious materials, Cem. Concr. Res. 37 (2007) 1440–1444.
[38] F.J. Ulm, M. Vandamme, C. Bobko, A. Ortega, K. Tai, C. Ortiz, Statistical indentation techniques for hydrated nanocomposites: concrete, bone, and shale, J. Am. Ceram. Soc. 90 (2007) 2677–2692.
[39] C. Plassard, E. Lesniewska, I. Pochard, A. Nonat, Investigation of the surface structure and elastic properties of calcium silicate hydrates at the nanoscale, Ultramicroscopy 100 (2004) 331–338.